Research Paper

Bispecific Antibody Conjugated Manganese-Based Magnetic Engineered Iron Oxide for Imaging of HER2/neu- and EGFR-Expressing Tumors

Shou-Cheng Wu[1,#], Yu-Jen Chen[1,#], Hsiang-Ching Wang[2], Min-Yuan Chou[2], Teng-Yuan Chang[3], Shyng-Shiou Yuan[4], Chiao-Yun Chen[5], Ming-Feng Hou[6], John Tsu-An Hsu[1,3,✉] and Yun-Ming Wang[1,7,✉]

1. Department of Biological Science and Technology, Institute of Molecular Medicine and Bioengineering, National Chiao Tung University, 75 Bo-Ai Street, Hsinchu 300, Taiwan
2. Biomedical Technology and Device Research Laboratories, Industrial Technology Research Institute, Hsinchu 310, Taiwan
3. Institute of Biotechnology and Pharmaceutical Research, National Health Research Institutes, Miaoli 350, Taiwan
4. Translational Research Center, Department of Medical Research, and Department of Obstetrics and Gynecology, Kaohsiung Medical University Hospital, Kaohsiung Medical University, Kaohsiung 807, Taiwan
5. Department of Medical Imaging, Kaohsiung Medical University Hospital, Kaohsiung 807, Taiwan
6. Cancer Center, Division of General and Gastroenterological Surgery, Department of Surgery, Kaohsiung Medical University Hospital, Kaohsiung, Taiwan
7. Department of Biomedical Science and Environmental Biology, Kaohsiung Medical University, Kaohsiung 807, Taiwan.

# These authors contributed equally to this study and share first authorship.

✉ Corresponding author: Yun-Ming Wang, Ph. D., Department of Biological Science and Technology, Institute of Molecular Medicine and Bioengineering, National Chiao Tung University, 75 Bo-Ai Street, Hsinchu 300, Taiwan. Tel: 886-3-5712121 ext. 56972; E-mail: ymwang@mail.nctu.edu.tw. John Tsu-An Hsu, Ph. D., Institute of Biotechnology and Pharmaceutical Research, National, Health Research Institutes, Miaoli 350, Taiwan. E-mail: tsuanhsu@nhri.org.tw

Abstract

The overexpression of HER2/neu and EGFR receptors plays important roles in tumorigenesis and tumor progression. Targeting these two receptors simultaneously can have a more widespread application in early diagnosis of cancers. In this study, a new multifunctional nanoparticles (MnMEIO-CyTE777-(Bis)-mPEG NPs) comprising a manganese-doped iron oxide nanoparticle core (MnMEIO), a silane-amino functionalized poly(ethylene glycol) copolymer shell, a near infrared fluorescence dye (CyTE777), and a covalently conjugated anti-HER2/neu and anti-EGFR receptors bispecific antibody (Bis) were successfully developed. *In vitro* T_2-weighted MR imaging studies in SKBR-3 and A431 tumor cells incubated with MnMEIO-CyTE777-(Bis)-mPEG NPs showed - 94.8 ± 3.8 and - 84.1 ± 2.8% negative contrast enhancement, respectively. Pharmacokinetics study showed that MnMEIO-CyTE777-(Bis)-mPEG NPs were eliminated from serum with the half-life of 21.3 mins. *In vivo* MR imaging showed that MnMEIO-CyTE777-(Bis)-mPEG NPs could specifically and effectively target to HER2/neu- and EGFR-expressing tumors in mice; the relative contrast enhancements were 11.8 (at 2 hrs post-injection) and 61.5 (at 24 hrs post-injection) fold higher in SKBR-3 tumors as compared to Colo-205 tumors. T_2-weighted MR and optical imaging studies revealed that the new contrast agent (MnMEIO-CyTE777-(Bis)-mPEG NPs) could specifically and effectively target to HER2/neu- and/or EGFR-expressing tumors. Our results demonstrate that MnMEIO-CyTE777-(Bis)-mPEG NPs are able to recognize the tumors expressing both HER2/neu and/or EGFR, and may provide a novel molecular imaging tool for early diagnosis of cancers expressing HER2/neu and/or EGFR.

Key words: bispecific antibody; MnMEIO; magnetic resonance imaging; HER2/neu; EGFR.

Introduction

Over the past few decades, magnetic resonance imaging (MRI) has offered the advantage of high resolution of contrast differences between tissues. [1, 2] Magnetic nanoparticles (MNPs) have been used for

biomedical applications due to their suitable sizes, high biocompatibility, superparamagnetic properties, and efficient targeting. [3-5] Recently, functional magnetic nanoparticles and enhanced targeting moieties, such as aptamers, peptides, and antibodies, were extensively used for tumor-associated applications. [6-10] Furthermore, antibody-induced cell apoptosis through the blockade and inhibition of growth factor-mediated signaling events has been applied for antibody-conjugated nanoparticles. [11, 12]

The developments and metastases of tumors are highly associated with certain proto-oncogenic protein receptor tyrosine kinases such as HER2/neu receptor, epidermal growth factor receptor (EGFR), or the mucin family proteins. [13-15] More than 20 kinds of monoclonal antibodies including those against HER/2neu and EGFR have been approved as treatment modalities for a variety of diseases. [16, 17] One of the major bottlenecks of current targeted cancer therapy is the heterogeneity of tumors such as switchable oncogenic receptor expression pattern or abnormal tumor microenvironment. [18-21] In line with this notion, varying expression levels of both HER2/neu and EGFR have been reported in several studies in breast, [22] colorectal, [23] and prostate cancers. [24] However, tumor heterogeneity and cancer cell plasticity may offer targeted therapy opportunities. For achieving precision medicine in the future, next-generation antibody based theranostics will overcome therapy resistance and provide more precision diagnostics even in treatment-induced heterogeneity situation. One possible way to improve binding selectivity, targeting efficiency, and diagnostic and therapeutic efficacy of targeted diagnosis and therapy is to simultaneously target multiple cancer-associated receptors. Currently, more than 70 drug candidates based on next-generation antibody technology platforms such as antibody–drug conjugates (ADCs) and bispecific antibodies (BsAbs) are in clinical development, although only two BsAbs, catumaxomab (anti-EpCAM × anti-CD3) and blinatumomab (anti-CD19 × anti-CD3), are approved for clinical use. [25, 26] Dual blockade of two different disease associated receptors with BsAb such as drug candidates, Duligotuzumab (anti-EGFR × anti-HER3) and MM-111 (anti-HER2 × anti-HER3), may overcome tumor heterogeneity, reduce the binding efficiency by steric hindrance between antibodies and antigens and increase potency or efficacy. [25, 27]

Using a bispecific Ab for nanoparticle conjugation not only simplifies conjugation process but also overcome the diverse expression patterns of individual receptors. The advantage of the bivalent binding modes of a bispecific Ab has been described in Fuh's review article. [28] Hence, we chose the bispecific antibody rather than coupling two different antibodies in the nanoparticle for this study. In addition, bispecific antibody is equally capable of triggering tumor uptake compared to conventional antibody, and has low retention time in the liver and kidneys. Bispecific antibody has been proven to be superior to monoclonal antibody in terms of specificity, sensitivity, and signal intensity. Hence, simultaneous targeting strategy by using bispecific antibody would significantly improve the quality and reliability in cancer imaging.

Improving the targeting efficacy of multifunctional nanoparticles is a growing trend for the development of contrast agents. We have previously developed a highly specific contrast agent system that comprises an iron oxide nanoparticle core coated with a flexible poly(ethylene glycol) which could mask the non-conjugated functional group to prevent nonspecific binding. [29] Adding on this system, bispecific antibody may provide a more efficient targeting tool for detection of HER2/neu- and EGFR-expressing tumors. Furthermore, the application of bispecific antibody as a targeting moiety on nanoparticles has not been reported, thus highlights the necessity and importance of this work. In this study bispecific antibody was functionalized and conjugated to the surface of MnMEIO-CyTE777-mPEG NPs to achieve preferential targeting to HER2/neu- and/or EGFR-expressing tumor cells. The efficacies of contrast agents (i.e., control NPs and bispecific antibody-conjugated NPs) were evaluated through cell cytotoxicity, flow cytometry, Prussian blue staining, *in vitro* optical and MR imaging, *in vivo* optical and MR imaging, and confocal fluorescent microscopy studies.

Materials and methods

Materials

Iron(III) acetylacetonate ([Fe(acac)$_3$], 99.9%), manganese(II) chloride (MnCl$_2$•4H$_2$O, 99%), methyl poly(ethylene glycol) (mPEG, M.W. = 2,000), oleic acid (90%), oleylamine (90%), *N*-ethyl-*N'*-(3-dimethylaminopropyl) carbodiimide (EDC), IR-783, fluorescein isothiocyanate (FITC), Prussian blue, and nuclear red fast were purchased from Sigma-Aldrich (St. Louis, MO, USA). Acryloyl chloride (96%) and *N*-Boc-ethylenediamine (98%) were purchased from Alfa Aesar (Ward Hill, MA, USA). (3-Aminopropyl) triethoxy silane (APTES, 98%) and benzyl ether were purchased from Fluka (Buchs, SG, Switzerland). (Benzotriazol-1-yloxy) tripyrrolidinophosphonium hexafluorophosphate (PyBOP) and *N*-hydroxybenzotriazole (HOBt) were purchased

from NovaBiochem (Beeston, NTH, UK). BCA (bicinchoninic acid) protein assay reagent kit was purchased from Pierce (Rockford, IL, USA). Molecular-porous membrane tubing (M.W. = 12~14 kDa and M.W. = 50 kDa) was purchased from Spectrum (Houston, TX, USA). The primary antibodies (mouse anti-EGFR and anti-β-actin) and secondary antibody (Rabbit polyclonal antibody to mouse IgG-H&L) were purchased from Abcam (Cambridge, MA, USA), and all the chemicals were used directly without any further purification unless otherwise stated.

Methods

The FT-IR analyses were performed using a Perkin-Elmer spectrum 2000 fourier transform infrared spectrometer (Boston, MA, USA). The ^{1}H NMR (300 MHz) spectra were recorded on a Varian Unity-300 NMR spectrometer (Palo Alto, CA, USA). The EDS spectra of MnMEIO NPs were obtained on a Hitachi S-3000N energy-dispersive spectrometer (Chiyoda-ku, TYO, Japan). Magnetic properties of the MnMEIO were studied with Model 7400 superconducting quantum interference devise (SQUID) magnetometer (Westerville, OH, USA) at fields ranging from -10 to 10 kOe and at 298 K. Relaxation time values (T_1 and T_2) of MnMEIO-CyTE777-(Bis)-mPEG NPs and control NPs (MnMEIO-CyTE777-mPEG, MnMEIO-CyTE777-(Her)-mPEG, MnMEIO-CyTE777-(Erb)-mPEG, and MnMEIO-CyTE777-(Erb+Her)-mPEG NPs) were measured to determine the relaxivities r_1 and r_2. The relaxation time values (T_1 and T_2) were measured by using various concentrations of nanoparticles. All measurements were made at 20 MHz and 37.0 ± 0.1 °C in PBS buffer using a Bruker NMS-120 Minispec relaxometer (Milton, ON, Canada). The relaxation time values were plotted against the concentrations of nanoparticles, to get six data points. Furthermore, the values of r_1 and r_2 were determined from the slope of the six data points. Hydrodynamic size and zeta potential were analyzed with Malvern Instruments DLS Nano ZS90 (Malvern, WOR, UK). Protein concentration was determined with NanoDrop ND-1000 UV-vis spectrometer (Wilmington, DE, USA). The flow cytometry experiments were carried out using a FACScan flow cytometer (San Jose, CA, USA). Optical imaging were acquired using an IVIS spectrum system (Hopkinton, MA, USA) and images collected were analyzed by Xenogen living image software version 3.0 (Hopkinton, MA, USA). The MR imaging was performed on Bruker 7.0 T MR imaging system (Ettlingen, Germany) with a volume coil used as radio frequency (RF) transmitter and receiver. The confocal fluorescent studies were performed using Leica TCS-SP5-X AOBS confocal microscope system (Bensheim, Germany).

The iron concentrations of pharmacokinetic studies were estimated by Agilent 7500 series inductively coupled plasma-mass spectrometer (Santa Clara, CA, USA).

Cells and animal model

All tumor cells (SKBR-3, A431, Colo-205, MCF-7, and MDA-MB-231) were cultured in RPMI or DMEM medium and supplemented with 10% fetal bovine serum (FBS) (GIBCO). All cells were cultured in a humidified incubator at 37 °C with 5% CO_2.

BALB/cAnN.Cg-Foxn1nu/CrlNarl mice (6-8 weeks old, female) were purchased from the National Laboratory Animal Center, Taipei, Taiwan. Animal experiments were performed in accordance with the institutional guidelines. SKBR-3 and Colo-205 tumor cells were subcutaneously injected to the flanks of nude mice (n = 4) in 100 µl PBS (1 × 10^6 cells) with matrigel. MR imaging experiments were performed two weeks after tumor implantation, at that time the tumors were measured approximately 500 mm^3 in volume.

Western blot assay

All tumor cells (SKBR-3, A431, and Colo-205) were washed twice with cold PBS and lysed on ice in RIPA buffer (10 mM PBS, 1% NP40, 0.1% sodium dodecyl sulfate (SDS), 5 mM EDTA, 0.5% sodium deoxycholate, and 1 mM sodium orthovanadate) with the presence of protease inhibitors and quantified using NanoDrop ND-1000 UV-vis spectrometer. Equal amount of protein (50-80 µg) was separated by SDS polyacrylamide gel, electrotransferred to polyvinylidene fluoride membranes (PVDF) and blocked in 5% nonfat dry milk in pH 7.5 Tris-buffer (100 mM NaCl, 50 mM Tris, 0.1% Tween-20). Membranes were immunoblotted overnight at 4 °C with anti-HER2/neu polyclonal antibody or anti-EGFR polyclonal antibody (1 : 1000 dilution) and anti β-actin (1 : 5000 dilution), followed by their respective horseradish peroxidase conjugated secondary antibody. Signals were detected by enhanced chemiluminescence. The β-actin was used as the internal control.

Determination of conjugation efficiency of antibody associated with NPs

The conjugation efficiency between bispecific antibody (Bis), Herceptin (Her), Erbitux (Erb), and both Herceptin and Erbitux (Erb+Her) with MnMEIO-CyTE777-mPEG NPs was determined by collecting unconjugated antibodies in the supernatant after centrifugal filtration of the antibody reaction mixture and measuring the concentration using NanoDrop ND-1000 UV-vis spectrometer. Data are represented as mean ± SD (n = 4).

In vitro cell cytotoxicity assay

All tumor cells (SKBR-3, A431, and Colo-205) were used to measure the *in vitro* cell cytotoxicity of MnMEIO-CyTE777-(Bis)-mPEG NPs. SKBR-3, A431, and Colo-205 cells were plated in 24-well plate at a density of 1×10^4 cells/well for 24 hrs and then MnMEIO-CyTE777-(Bis)-mPEG NPs (10 µg/ml) were added at the desired concentrations of Fe (0.1, 0.2, 0.4, 0.8, and 1.6 mM) for 24 hrs. Culture supernatants were removed and cells washed three times with PBS, then cell viability was estimated using the MTT conversion test. Briefly, MTT (100 µl) solution was added to each well. After incubation for 2 hrs, each well was treated with DMSO (50 µl) for 3 to 5 mins. Absorption at 570 nm was measured on a plate reader. The result was represented as mean ± SD % (n = 4) with the untreated cells (control) as 100% viability.

Flow cytometry assay

All tumor cells (SKBR-3, A431, and Colo-205) were collected in microcentrifuge tubes (1×10^6 cells each). These tumor cells were incubated with MnMEIO-FITC-(Bis)-mPEG NPs and control NPs (MnMEIO-FITC-mPEG, MnMEIO-FITC-(Her)-mPEG, MnMEIO-FITC-(Erb)-mPEG, and MnMEIO-FITC-(Erb+Her)-mPEG NPs) (10 µg/ml) for 1 hr at 37 °C or 4 °C, washed three times with PBS, and then resuspended by 1 ml PBS in FACS tube. Finally, the immunofluorescence of viable cells was measured and their fluorescent intensity was analyzed with the FACScan flow cytometer (*San Jose, CA*, USA).

Prussian blue staining assay

All tumor cells (SKBR-3, A431, and Colo-205) were seeded at a density of 2×10^5 cells/well on cover glasses (24 × 24 mm) and allowed to grow for 24 hrs. Then tumor cells were incubated with MnMEIO-CyTE777-(Bis)-mPEG NPs and control NPs (MnMEIO-CyTE777-mPEG, MnMEIO-CyTE777-(Her)-mPEG, MnMEIO-CyTE777-(Erb)-mPEG, and MnMEIO-CyTE777-(Erb+Her)-mPEG NPs) (10 µg/ml) for 1 hr at 37 °C. Slides were stained with Prussian blue to detect Fe deposition. Hypodermic tumor sections mounted on slides were stained with a 1 : 1 mixture of 2% potassium ferrocyanide and 2% hydrochloric acid for 30 mins at room temperature. The slides were rinsed with PBS buffer, dehydrated, and photographed.

In vitro optical imaging study

SKBR-3, A431, Colo-205, MCF-7, and MDA-MB-231 tumor cells were used to measure the specific binding of MnMEIO-CyTE777-(Bis)-mPEG NPs and control NPs (MnMEIO-CyTE777-mPEG, MnMEIO-CyTE777-(Her)-mPEG, MnMEIO-CyTE777-(Erb)-mPEG, and MnMEIO-CyTE777-(Erb+Her)-mPEG NPs). SKBR-3, A431, and Colo-205 cells were plated in 96-well plate at a density of 1×10^4 cells/well for 24 hrs and then incubated with the NPs (10 µg/ml) for 1 hr at 37 °C. After incubation, the supernatants were removed and cells washed three times with PBS. The optical imaging was then acquired using an IVIS spectrum system. The emission at 820 nm was measured with an optimal excitation wavelength of 745 nm (1 sec, F-stop = 2 and small binning). Data is represented as mean ± SD (n = 4). Optical intensity of cells incubated with different probes were compared by two-way ANOVA. $P \le 0.05$ is considered significant. Bouferroni correction was applied for P values when multiple comparisons were made.

In vitro MR imaging study

SKBR-3, A431, and Colo-205 cells in 96-well plated at a density of 1×10^4 cells, were incubated with MnMEIO-CyTE777-(Bis)-mPEG NPs and control NPs (MnMEIO-CyTE777-mPEG, MnMEIO-CyTE777-(Her)-mPEG, MnMEIO-CyTE777-(Erb)-mPEG, and MnMEIO-CyTE777-(Erb+Her)-mPEG NPs) (10 µg/ml) for 1 hr at 37 °C and then washed three times with PBS. All samples were scanned by a fast gradient echo pulse sequence (7.0 T) and data were represented as mean ± SD (n = 4). The contrast enhancement (%) was calculated by the following equation (1) [30]

$$\text{Enhancement (\%)} = [(SI_{post} - SI_{pre}) / SI_{pre}] \times 100 \quad (1)$$

where SI_{post} is the value of signal intensity of tumor cells treated with MnMEIO-(Bis)-mPEG NPs and control NPs (MnMEIO-mPEG, MnMEIO-(Her)-mPEG, MnMEIO-(Erb)-mPEG, and MnMEIO-(Erb+Her)-mPEG NPs), and SI_{pre} is the value of signal intensity of tumor cells alone. Contrast enhancement of cells incubated with different probes were compared by two-way ANOVA. $P \le 0.05$ is considered significant. Bouferroni correction was applied for P values when multiple comparisons were made.

Pharmacokinetic study

Nude mice bearing SKBR-3 and Colo-205 tumors (approximately 500 mm³) were anesthetized and injected via tail veins with MnMEIO-CyTE777-(Bis)-mPEG NPs (10 mg/kg). About 10 µl blood samples were collected at pre-injection at pre-injection and various time points (2, 5, 10, 30, 60, 180, 360, 720, and 1440 mins) post-injection. In addition, the iron concentration was estimated by inductively coupled plasma-mass spectrometer (ICP-MS). Data is represented as mean ± SD (n = 4, for each group). Serum concentration of probes at different time point was compared by Wilcoxon rank sum test. $P \le 0.05$ is considered significant.

Confocal fluorescent microscopy

SKBR-3, A431, and Colo-205 cells were seeded at a density of 1×10^4 cells/well on cover glasses (24 × 24 mm) and allowed to grow for 24 hrs. Then tumor cells were incubated with MnMEIO-FITC-(Bis)-mPEG NPs (10 μg/ml) for 1 hr at 37 °C or 4 °C, washed three times with PBS, and fixed with 4% formaldehyde solution for 30 mins at room temperature. Cell nuclei and cytoplasm were stained with 4′-6-diamidino-2-phenylindole (DAPI, blue) and HiLyte Fluor™ 594 acid (red), respectively. Cover glasses containing fixed cells were mounted in a mixture of PBS and glycerol (1 : 1) on a microscope slide and the cells were observed using confocal imaging system.

In vivo optical imaging study

Nude mice bearing SKBR-3 and Colo-205 tumors (approximately 500 mm³) were anesthetized and injected via tail veins with MnMEIO-CyTE777-mPEG and MnMEIO-CyTE777-(Bis)-mPEG NPs (10 mg/kg), respectively. Optical imaging was acquired at pre-injection and various time points (2, 8, 24, and 96 hrs) post-injection using an IVIS spectrum system. Then the emission at 820 nm was measured with an optimal excitation wavelength of 745 nm (1 sec, F-stop = 2 and small binning). Data is represented as mean ± SD (n = 4). Signal intensities between tumors at different time point were compared by Wilcoxon rank sum test. P ≤ 0.05 is considered significant.

In vivo MR imaging study

Nude mice bearing SKBR-3 and Colo-205 tumors were anesthetized by pentobarbital when the tumor size reached approximately 500 mm³. MnMEIO-CyTE777-(Bis)-mPEG NPs (10 mg/kg) were injected via the tail veins to the mice. All the mice were measured using a T_2-weighted fast spin-echo sequence 7.0 T imaging for every 3 mm sectioning thickness. Images were acquired at pre-injection and various time points (2 and 24 hrs) post-injection. Data is represented as mean ± SD (n = 4). Statistical analysis of Wilcoxon rank sum test was used to evaluate the statistical significance. The contrast enhancement (%) was calculated by the equation (1), where SI_{post} is the value of signal intensity of the tumor cells after contrast agent injection and SI_{pre} is the value of signal intensity of the tumor cells before contrast agent injection.

Histological analysis

Tumor-bearing mice were sacrificed after MR imaging studies, SKBR-3 and Colo-205 tumor biopsies were fixed in 10% formalin and embedded in paraffin. Sections (6-10 μm) were cut from representative tumors. Slides were evaluated by Prussian blue and nuclear fast red staining for iron and the cytoplasm and nucleus recognition, respectively. After staining, all sections were imaged and captured with a microscope.

Results and Discussion

Production of recombinant bispecific antibody

The variable domains of heavy (V_H) and light (V_L) chains of anti-EGFR (Erbitux) and anti-HER2/neu (Herceptin) were linked via (Gly4Ser)3 to form scFv (Erbitux) and scFv (Herceptin), respectively. The bispecific fragment was then generated by linking scFv (Erbitux) and scFv (Herceptin) with a flexible peptide linker, ASTGS, and cloned into the 5′ region of the human IgG1 Fc in pFUSE-hIgG1e4-Fc vector to form an Fc-fusion construct (Fig. 1A). The recombinant tetravalent bispecific antibody (Bis) (Fig. 1B) was produced by CHO-RD cells stably transfected with the expression construct, and purified from cell culture supernatants. A stable clone that highly expressed the bispecific antibody was confirmed by Western blot (Fig. 1C). Then, the purity of the bispecific antibody recombinant protein was assessed by SDS-PAGE analysis under both reducing and non-reducing conditions (Fig. 1D). Furthermore, the binding affinity study of bispecific antibody for EGFR and HER2/neu receptors was measured in enzyme-linked immunosorbent assay experiments. The binding affinity (KD value) of bispecific Ab was ~10 and ~3 nM for soluble EGFRv3-ECD-hFc and Her2-ECD-hFc, respectively (Fig. S1†).

Synthesis of MnMEIO-CyTE777-(Bis)-mPEG NPs and control NPs (MnMEIO- CyTE777-mPEG, MnMEIO-CyTE777-(Her)-mPEG, MnMEIO-CyTE777-(Erb)- mPEG, and MnMEIO-CyTE777-(Erb+Her)-mPEG NPs)

Previously, we have developed a nanoparticle system (MnMEIO-mPEG NPs) which can prevent non-specific binding between nanoparticles and cell membranes. [29] In this study, the nanoparticle was conjugated with the bispecific antibody capable of binding to two tumor-associated receptors [31, 32] for lesion detection. The mPEG of the MnMEIO-CyTE777-(Bis)-mPEG NPs reduced the electrostatic interaction between NPs and negatively charged cell membranes and avoided the non-specific binding. The manganese-based magnetic engineered iron oxide (MnMEIO) NPs with approximately 2.2 of Fe/Mn ratio (Fig. S2†) were synthesized using a non-hydrolytic thermal decomposition process. Silane-NH2-mPEG was synthesized via Michael addition of N-Boc-ethylenediamine to methoxypoly (ethylene glycol) acrylate (mPEG-Ac), and after Boc

deprotection to (3-aminopropyl) triethoxy silane acrylate (APTES-Ac). Based on this, silane-NH$_2$-mPEG coated NPs (MnMEIO-mPEG NPs) were prepared through a ligand-exchange reaction using oleic acid, oleyl amine-stabilized MnMEIO NPs, and silane-NH$_2$-mPEG. After successful ligand exchange reaction, the surface property of NPs changed from hydrophobic to hydrophilic. TEM analyses revealed that the average diameter of MnMEIO-mPEG NPs was 9.1 ± 0.3 nm (Fig. 2).
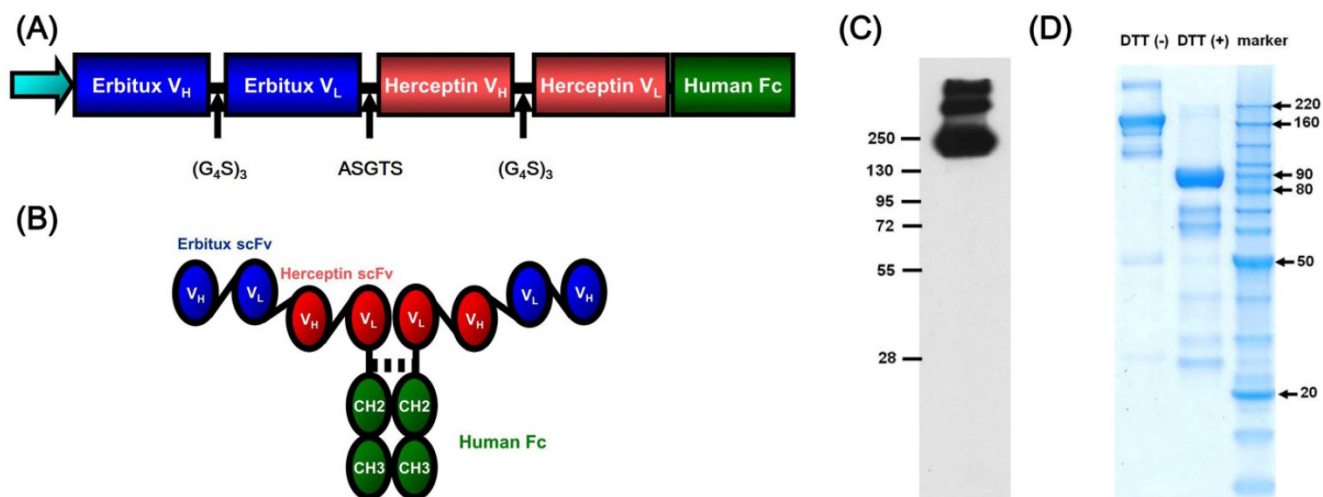

Fig. 1. Schematic diagram of tetravalent bispecific antibody. (A) Structure of scFv and human Fc domains, and (B) assembled tetravalent bispecific antibody. Purification and structural characterization of tetravalent bispecific antibody (Bis). (C) Confirmation of tetravalent bispecific antibody expression by Western blot analysis. (D) Purified tetravalent bispecific antibody were electrophoresed on SDS-PAGE under non-reducing condition (DTT (-)) and reducing conditions (DTT (+)).
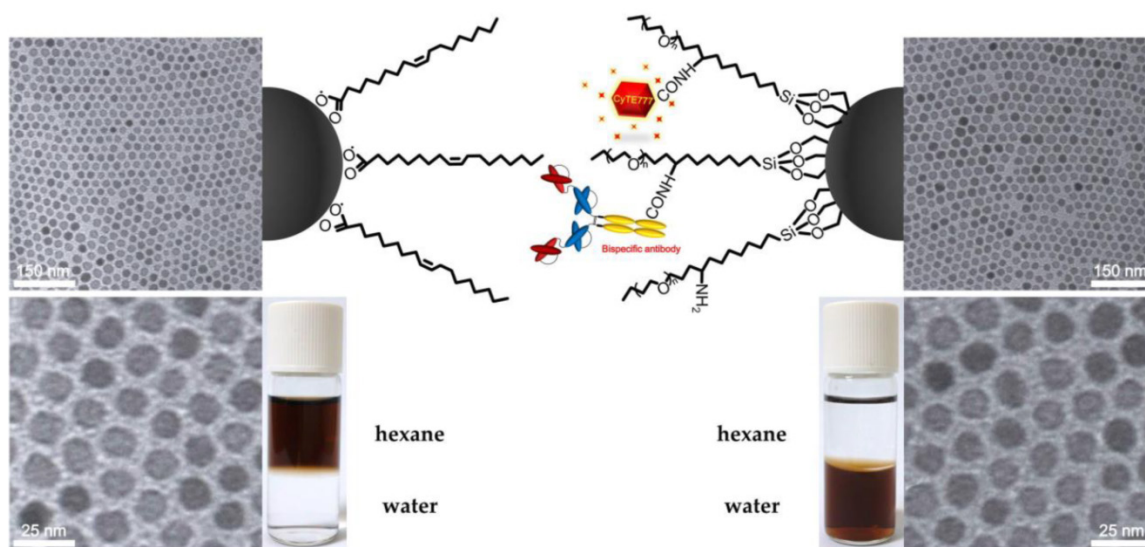

Fig. 2. TEM images and schematic representation of MnMEIO NPs conjugated with (right) or without (left) mPEG, CyTE777 and the bispecific antibody. The core size of MnMEIO NPs was 9.1 ± 0.3 nm. Then, the organic and aqueous dispersions of nanoparticles were also shown.

Followed by the syntheses of MnMEIO-mPEG, MnMEIO-CyTE777-(Bis)-mPEG NPs and control NPs (MnMEIO-CyTE777-(Her)-mPEG, MnMEIO-CyTE777-(Erb)-mPEG, and MnMEIO-CyTE777-(Erb+Her)-mPEG NPs), the carboxylic acid in CyTE777 dye was briefly activated with EDC/NHS and the activated CyTE777 was conjugated to MnMEIO-mPEG NPs to yield MnMEIO-CyTE777-mPEG NPs. In this design, CyTE777 could be applied for *in vitro* and *in vivo* optical imaging due to low autofluorescence and deep tissue penetration.

The -COOH moiety of antibody was then activated by EDC/NHS. MnMEIO-CyTE777-mPEG NPs were mixed with activated antibody to yield MnMEIO-CyTE777-(Bis)-mPEG and control NPs, respectively. In this setting, the antibody could target either HER2/neu- or EGFR-expressing tumor cells (Fig. 2). As shown in Table S1†, the dynamic light-scattering (DLS) measurement indicated that MnMEIO-CyTE777-mPEG NPs had a relatively narrow size distribution of 27.4 ± 2.1 nm. The magnetization curve obtained at room temperature showed that

the saturation magnetization (Ms) and coercivity of MnMEIO-CyTE777-(Bis)-mPEG NPs obtained from the magnetization curve were 83.3 emu/g and 6.6 Oe, respectively (Fig. S3†). These results indicated the NPs had no coercive force, and showed superparamagnetic behavior. Upon conjugation with antibody and CyTE777, the size of MnMEIO-CyTE777-(Bis)-mPEG NPs and control NPs (MnMEIO-CyTE777-(Her)-mPEG, MnMEIO-CyTE777-(Erb)-mPEG, and MnMEIO-CyTE777-(Erb+Her)-mPEG NPs) increased to 42.5 ± 1.8, 45.1 ± 1.4, 38.7 ± 0.8, and 43.2 ± 0.4 nm, respectively. This increase indicated that antibody and CyTE777 were coupled to the MnMEIO-mPEG and formed MnMEIO-CyTE777-(Bis)-mPEG NPs and control NPs. Furthermore, the zeta-potential values of MnMEIO-CyTE777-(Bis)-mPEG NPs and control NPs (MnMEIO-CyTE777-(Her)-mPEG, MnMEIO-CyTE777-(Erb)-mPEG, and MnMEIO-CyTE777-(Erb+Her)-mPEG NPs) were - 3.8 ± 0.3, + 15.2 ± 1.6, - 1.9 ± 0.2, - 1.3 ± 0.1, and - 3.1 ± 0.2 mV, respectively. These results indicated that the zeta-potential values were reduced for MnMEIO-CyTE777-(Bis)-mPEG NPs and control NPs at pH 7.0, and this decrease can be attributed to the shielding effects of mPEG groups. [29] The negative zeta-potential value (- 3.8 ± 0.3 mV) obtained for MnMEIO-CyTE777-(Bis)-mPEG NPs prevented non-specific binding to HER2/neu- and/or EGFR-expressing tumor cells. The r_2/r_1 ratios of MnMEIO-CyTE777-(Bis)-mPEG NPs and control NPs (MnMEIO-CyTE777-(Her)-mPEG, MnMEIO-CyTE777-(Erb)-mPEG, and MnMEIO-CyTE777-(Erb+Her)-mPEG NPs) measured at 20 MHz and 37.0 ± 0.1 °C were 6.8, 6.9, 6.7, 6.3, and 6.2, respectively (Table S1†). Moreover, the loading capacities of antibody in MnMEIO-CyTE777-(Bis)-mPEG NPs and control NPs (MnMEIO-CyTE777-(Her)-mPEG, MnMEIO-CyTE777-(Erb)-mPEG, and MnMEIO-CyTE777-(Erb+Her)-mPEG NPs) measured by NanoDrop ND-1000 UV-vis spectrometer were 76.8 ± 1.9, 81.2 ± 1.3, 84.5 ± 2.4, and 79.1 ± 1.8 µg/mg NPs, respectively. Furthermore, stabilities of MnMEIO-CyTE777-(Bis)-mPEG and MnMEIO-CyTE777-mPEG NPs were test for 10 days in PBS, medium + 10% FBS, and FBS. (Fig. S4†) The hydrodynamic sizes of MnMEIO-CyTE777-(Bis)-mPEG and MnMEIO-CyTE777-mPEG NPs were stably consistent from initial day (day 0) to 10th day. These results demonstrated that the nanoparticles would not to aggregate and are stable even for 10 days long.

Cell cytotoxicity

Cytotoxicity is a key parameter for applying contrast agents in biomedical applications. We used MTT assay to evaluate cytotoxicity of

MnMEIO-CyTE777-(Bis)-mPEG NPs against SKBR-3 (HER2/neu⁺), A431 (EGFR⁺), and Colo205 (HER2/neu⁻ and EGFR⁻) tumor cells. As shown in Fig. S5†, these cells displayed high viability (more than 95%) even treated with high concentrations of NPs. Thus these NPs are relatively nontoxic.

Binding specificity of NPs to HER2/neu- and EGFR-expressing tumor cells

After treatments of MnMEIO-FITC-(Bis)-mPEG NPs and control NPs (MnMEIO-FITC-mPEG, MnMEIO-FITC-(Her)-mPEG, MnMEIO-FITC-(Erb)-mPEG, and MnMEIO-FITC-(Erb+Her)-mPEG NPs), the tumor cells were subjected to flow cytometry in order to confirm the binding specificity of NPs to HER2/neu and EGFR receptors on tumor cells that expressed high levels of HER2/neu and EGFR. As shown in Fig. S6†, HER2/neu expression levels in A431 and SKBR-3 were moderate and significantly high, respectively. [33, 34] On the other hand, EGFR expression levels in A431 and SKBR-3 were high and moderate, respectively. However, neither HER2/neu nor EGFR was detectable in Colo-205 tumor cells. Before flow cytometric analysis, the NPs were fluorescently labelled with FITC to provide fluorescent signal adequate for flow cytometer. In flow cytometric studies, three types of tumor cells, SKBR-3 (high HER2/neu expression and moderate EGFR expression), A431 (moderate HER2/neu and high EGFR expression), and Colo-205 (expressed neither HER2/neu nor EGFR) were incubated with MnMEIO-FITC-(Bis)-mPEG NPs or control NPs for 1 hr at 37 °C and 4 °C and cell-associated fluorescence was measured by a flow cytometer (Fig. 3 and Fig. S5†). Compared to control NPs, MnMEIO-FITC-(Bis)-mPEG NPs clearly bound to SKBR-3 tumor cells that strong fluorescence intensity was noted on the cells (Fig. 3A). These results indicated that high fluorescence intensity in SKBR-3 tumor cells incubated with MnMEIO-FITC-(Bis)-mPEG NPs represented a high binding activity as compared to that from control NPs. Furthermore, as shown in Fig. 3B, moderate fluorescence intensity was observed in A431 tumor cells incubated with MnMEIO-FITC-(Bis)-mPEG NPs. Notably, MnMEIO-FITC-(Bis)-mPEG NPs showed a higher binding activity to high EGFR-expressing A431 tumor cells than that of MnMEIO-FITC-(Erb+Her)-mPEG and MnMEIO-FITC-(Her)-mPEG NPs, but demonstrated lower binding activity than that of MnMEIO-FITC-(Erb)-mPEG NPs. In contrast, only slightly fluorescence shifts were recorded from Colo-205 tumor cells when treated with either MnMEIO-FITC-(Bis)-mPEG NPs or control NPs (Fig. 3C). As Colo-205 tumor cells expressed very low levels of HER2/neu and EGFR receptors, all the NPs

bound poorly to Colo-205 tumor cells. In addition, the same experiments were performed at 4 °C to confirm the tumor targeting of bispecific antibody to the membrane-bound HER2/neu and EGFR receptors (Fig. S7†). In this experiment, strong and moderate fluorescence intensities were observed in SKBR-3 and A431 tumor cells treated with MnMEIO-FITC-(Bis)-mPEG NPs, but only poor fluorescence shift was noted in Colo-205 tumor cells. These results are consistent with the flow cytometry studies carried out at 37 °C. In addition, blocking study were also carried out to further proving the binding specificity of NPs to HER2/neu and EGFR receptors on tumor cells. Tumor cells pretreated with excess Herceptin, Erbitux, and both antibodies, respectively, for 1 hr at 37 °C, followed by incubation with MnMEIO-CyTE777-(Bis)-mPEG NPs. As shown in Fig. S8†, SKBR-3 tumor cells pretreated with Herceptin decrease 40.9% fluorescence intensity in comparison of non-pretreated group. Similarly, compared to non-pretreated group, 56.9% decrease was observed when A431 tumors were pretreated with Erbitux. Furthermore, MCF-7 (expressing moderate levels of HER2/neu and high EGFR) and MDA-MB-231 (expressing moderate HER2/neu level and high level of EGFR) tumor cells were also use for this study. There were 22.5% and 44.9%, respectively, decrease when tumor cells pretreated with Erbitux. These results confirmed the binding specificity of bispecific antibodies-modified nanoparticles. Furthermore, dense intracellular iron labeling in SKBR-3 tumor cells, moderate iron labeling in A431 tumor cells, and very faint iron labeling in Colo-205 tumor cells were consistently noted (Fig. S9†). These results are consistent with flow cytometry analyses, indicating that higher binding activity was achieved when MnMEIO-CyTE777-(Bis)-mPEG NPs were used.

In vitro optical and MR imaging

To further test the binding activity, SKBR-3, A431, and Colo-205 tumor cells were treated with MnMEIO-CyTE777-(Bis)-mPEG NPs and control NPs (MnMEIO-CyTE777-mPEG, MnMEIO-CyTE777-(Her)-mPEG, MnMEIO-CyTE777-(Erb)-mPEG, and MnMEIO-CyTE777-(Erb+Her)-mPEG NPs) at 37 °C for 1 hr. The fluorescence intensities in a multi-well format were obtained by the IVIS spectrum system. As shown in Fig. 4A, when incubated with MnMEIO-CyTE777-(Bis)-mPEG NPs, high fluorescence intensity was found in SKBR-3 tumor cells, and moderate fluorescence intensity was showed in A431 tumor cells. When compared to Colo-205, SKBR-3 cells displayed significantly higher fluorescent intensities after incubation with MnMEIO-CyTE777-(Bis)-mPEG NPs and control NPs (MnMEIO-CyTE777-mPEG, MnMEIO-CyTE777-(Her)-mPEG, MnMEIO-CyTE777-(Erb)-mPEG, and MnMEIO-CyTE777-(Erb+Her)-mPEG NPs) (P = 0.0086, 0.0124, 0.0216, and 0.0173, respectively). Similarly, A431 showed significantly higher fluorescent intensities after incubation with MnMEIO-CyTE777-(Bis)-mPEG NPs and control NPs (MnMEIO-CyTE777-mPEG, MnMEIO-CyTE777-(Her)-mPEG, MnMEIO-CyTE777-(Erb)-mPEG, and MnMEIO-CyTE777-(Erb+Her)-mPEG NPs) (P = 0.0195, 0.0223, 0.0072, and 0.0208, respectively). In addition, MCF-7 and MDA-MB-231 tumor cells were also used for this study. As shown in Fig. S10†, MCF-7 and MDA-MB-231 tumor cells displayed high fluorescence intensity when incubated with MnMEIO-CyTE777-(Bis)-mPEG NPs. Then the intensities decreased while incubated with the control NPs. These results indicated that bispecific antibody-conjugated NPs could specifically bind to either HER2/neu- or EGFR-expressing tumor cells.
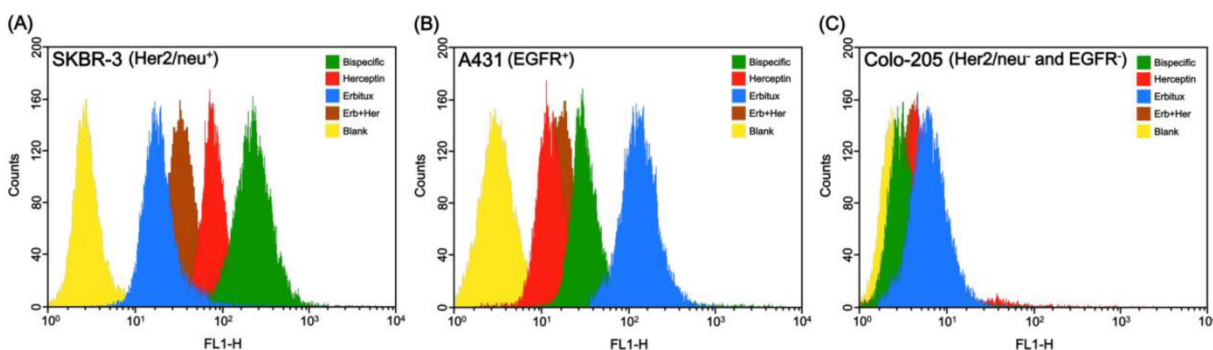

Fig. 3. Binding activity of MnMEIO-FITC-(Bis)-mPEG NPs and the control NPs (MnMEIO-FITC-mPEG (Blank), MnMEIO-FITC-(Her)-mPEG, MnMEIO-FITC-(Erb)-mPEG, and MnMEIO-FITC-(Erb+Her)-mPEG NPs) to (A) SKBR-3, (B) A431, and (C) Colo-205 cells. In these experiments NPs (10 μg/mL) were incubated with cells for 1 hr at 37 °C. Cell-associated fluorescent intensities were analyzed with a FACScan flow cytometer Binding activity of MnMEIO-FITC-(Bis)-mPEG NPs and the control NPs (MnMEIO-FITC-mPEG (Blank), MnMEIO-FITC-(Her)-mPEG, MnMEIO-FITC-(Erb)-mPEG, and MnMEIO-FITC-(Erb+Her)-mPEG NPs) to (A) SKBR-3, (B) A431, and (C) Colo-205 cells. In these experiments NPs (10 μg/mL) were incubated with cells for 1 hr at 37 °C. Cell-associated fluorescent intensities were analyzed with a FACScan flow cytometer.
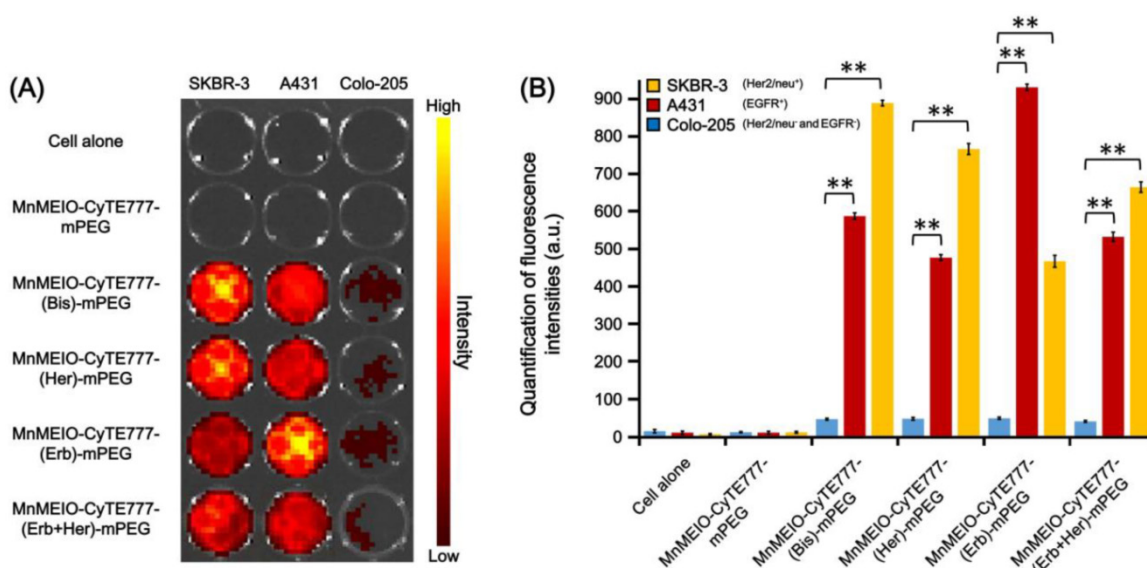
Fig. 4. *In vitro* optical imaging of SKBR-3, A431, and Colo-205 tumor cells after the treatment with MnMEIO-CyTE777-(Bis)-mPEG NPs and control NPs (MnMEIO-CyTE777-mPEG, MnMEIO-CyTE777-(Her)-mPEG, MnMEIO-CyTE777-(Erb)-mPEG, and MnMEIO-CyTE777-(Erb+Her)-mPEG NPs). In these experiments NPs (10 µg/mL) were incubated with cells for 1 hr at 37 °C. (A) Fluorescence images in a multi-well format were obtained by the IVIS spectrum system; (B) Quantitative analysis of fluorescence intensities of (A).

In vitro MR imaging was performed in a 7.0 T MR imaging system to demonstrate the binding specificity of MnMEIO-CyTE777-(Bis)-mPEG NPs in tumor cells. SKBR-3, A431, and Colo-205 tumor cells were treated with MnMEIO-CyTE777-(Bis)-mPEG NPs and control NPs (MnMEIO-CyTE777-mPEG, MnMEIO-CyTE777-(Her)-mPEG, MnMEIO-CyTE777-(Erb)-mPEG, and MnMEIO-CyTE777-(Erb+Her)-mPEG NPs) for 1 hr at 37 °C, and the corresponding MR negative contrast enhancement was quantified. As shown in Fig. 5, *in vitro* T_2-weighted MR images for SKBR-3 tumor cells showed negative contrast enhancements of - 1.2 ± 0.3, - 94.8 ± 3.8, - 85.4 ± 3.3, - 64.7 ± 3.6%, and - 79.6 ± 2.1% respectively when treated with MnMEIO-CyTE777-mPEG, MnMEIO-CyTE777-(Bis)-mPEG, MnMEIO-CyTE777-(Her)-mPEG, MnMEIO-CyTE777-(Erb)-mPEG, and MnMEIO-CyTE777-(Erb+Her)-mPEG NPs, while A431 tumor cells exhibited negative contrast enhancements of - 1.7 ± 0.1, - 84.1 ± 2.8, - 70.9 ± 2.7, - 89.2 ± 4.6%, and - 76.3 ± 1.3% respectively when treated with the same sets of NPs. When compared to Colo-205, SKBR-3 cells displayed significantly higher negative contrast enhancements after incubation with MnMEIO-CyTE777-(Bis)-mPEG NPs and control NPs (MnMEIO-CyTE777-mPEG, MnMEIO-CyTE777-(Her)-mPEG, MnMEIO-CyTE777-(Erb)-mPEG, and MnMEIO-CyTE777-(Erb+Her)-mPEG NPs) (P = 0.0139, 0.0166, 0.0229, and 0.0182, respectively). Similarly, A431 showed significantly higher negative contrast enhancements after incubation with MnMEIO-CyTE777-(Bis)-mPEG NPs and control NPs (MnMEIO-CyTE777-mPEG,

MnMEIO-CyTE777-(Her)-mPEG, MnMEIO-CyTE777-(Erb)-mPEG, and MnMEIO-CyTE777-(Erb+Her)-mPEG NPs) (P = 0.0171, 0.0206, 0.0143, and 0.0188, respectively). By comparing these results, it is clear that high or moderate negative contrast enhancements observed for SKBR-3 or A431 tumor cells indicated higher binding activity of MnMEIO-CyTE777-(Bis)-mPEG NPs for HER2/neu and EGFR receptors.

Confocal fluorescence imaging analysis

To further characterize the *in vitro* specificity of MnMEIO-FITC-(Bis)-mPEG NPs, we performed immunofluorescence staining in which tumor cells were incubated with MnMEIO-FITC-(Bis)-mPEG NPs at 37 °C and 4 °C, respectively (Figs. 6 and S7†, respectively). Fig. 6 showed substantial variations of FITC fluorescence signals observed for SKBR-3, A431, and Colo-205 tumor cells at 37 °C. Although all three cells showed green fluorescence signals, the green fluorescence intensities observed in SKBR-3 and A431 tumor cells were clearly stronger than that found in Colo-205 tumor cells. These results can be attributed to the higher expression levels of HER2/neu and EGFR in SKBR-3 and A431 tumor cells than that in Colo-205 tumor cells. In addition, endocytosis is known as a general entry mechanism for various extracellular materials [35-37] and is hindered when incubations are carried out at low temperature (4 °C instead of 37 °C). In this study, experiments were also performed at 4 °C to confirm the targeting capability of bispecific antibody (Fig. S11†). The green fluorescence was reduced and limited to cell membranes of

SKBR-3 and A431 tumor cells. However, green fluorescence was still not found in Colo-205 tumor cells. These results indicated that endocytosis was the mechanism of uptake of MnMEIO-FITC-(Bis)-mPEG

NPs at 37 °C, and MnMEIO-FITC-(Bis)-mPEG NPs can serve as an efficient and specific targeting contrast agent for the identification of both HER2/neu- and EGFR-expressing tumors.
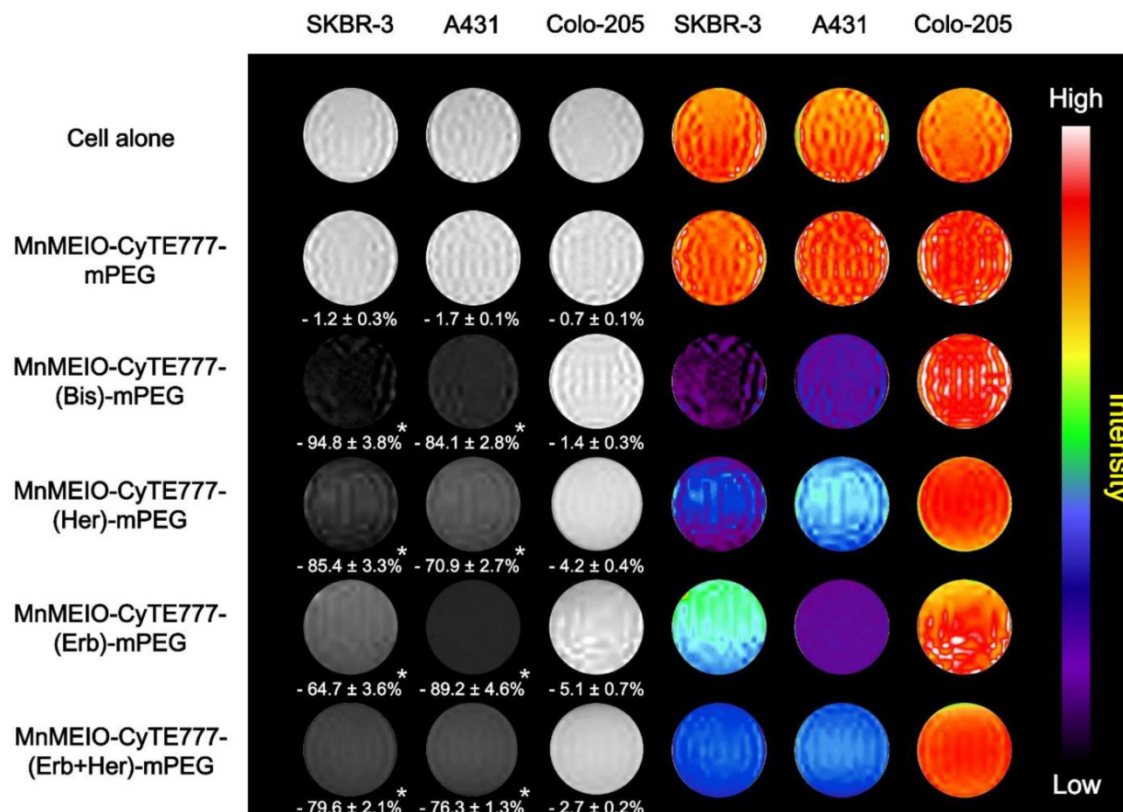

Fig. 5. The *in vitro* T_2-weighted images of SKBR-3, A431, and Colo-205 tumor cells after treatment with MnMEIO-CyTE777-(Bis)-mPEG NPs and control NPs (MnMEIO-CyTE777 -mPEG, MnMEIO-CyTE777-(Her)-mPEG, MnMEIO-CyTE777-(Erb)-mPEG, and MnMEIO-CyTE777-(Erb+Her)-mPEG NPs). In these experiments, NPs (10 µg/mL) were incubated with cells for 1 hr at 37 °C. MR imaging was performed with a 7.0 T MR imaging scanner.
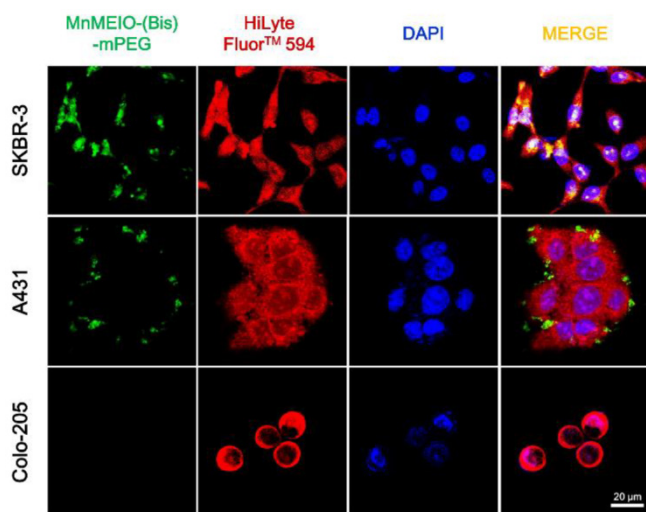
Fig. 6. Confocal microscopy images of SKBR-3, A431, and Colo-205 tumor cells incubated with MnMEIO-FITC-(Bis)-mPEG NPs (10 µg/mL) for 1 hr at 37 °C. HiLyte FluorTM 594 stained the cytoplasm in red and DAPI stained the nuclei in blue.

Pharmacokinetic study

The half-lives of MnMEIO-CyTE777-(Bis)-mPEG and control NPs (MnMEIO-CyTE777-mPEG NPs) in blood circulation were investigated using nude mice bearing subcutaneous SKBR-3 and Colo-205 tumor xenografts. Blood was drawn sequentially from the tail veins at pre-injection and various time points (2, 5, 10, 30, 60, 180, 360, 720, and 1440 mins) post-injection. The blood samples were assessed for iron concentration using ICP-MS. Half-lives were determined by monoexponential fitting of the normalized variance of blood iron concentration over time. The results of blood clearance were shown in Fig. 7. After injection of NPs, the blood iron concentration gradually decreased from the maximal concentration (263.46 µg/ml, at 5 mins for MnMEIO-CyTE777-(Bis)-mPEG NPs and, 268.49 µg/ml, at 10 mins for MnMEIO-CyTE777-mPEG NPs, respectively) to the lowest concentration (3.69 µg/ml, at 720 mins for MnMEIO-CyTE777-(Bis)-mPEG NPs and, 7.62 µg/ml, at 1440 mins for MnMEIO-CyTE777-mPEG NPs, re-

spectively). The half-lives of MnMEIO-CyTE777-(Bis)-mPEG and MnMEIO-CyTE777-mPEG NPs in blood circulation were accordingly calculated as 21.3 ± 0.2 and 46.6 ± 1.1 mins, respectively.
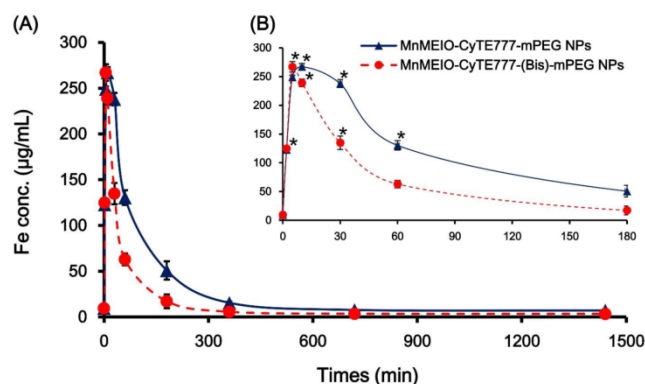

Fig. 7. (A) Pharmacokinetics of MnMEIO-CyTE777-(Bis)-mPEG and control NPs (MnMEIO-CyTE777-mPEG NPs) in nude mice bearing subcutaneous tumor xenografts of SKBR-3 and Colo-205 tumor cells. The blood clearances were compared at pre-injection and various time points (2, 5, 10, 30, 60, 180, 360, 720, and 1440 mins) post-injection; (B) iron concentrations upon various time points based on (A).

In vivo optical imaging study

To compare the utility of MnMEIO-CyTE777-mPEG and MnMEIO-CyTE777-

(Bis)-mPEG NPs for *in vivo* optical imaging, nude mice bearing subcutaneous SKBR-3 and Colo-205 tumor xenografts were intravenously injected MnMEIO-CyTE777-mPEG and MnMEIO-CyTE777-(Bis)-mPEG NPs, and then subjected to whole body optical imaging by IVIS spectrum system. As shown in Fig. 8A, a significant fluorescence enhancement was observed in SKBR-3 tumors and the fluorescence signal intensity persists for 96 hrs with a gradual attenuation. However, there was no obvious fluorescence enhancement in Colo-205 tumors. The fluorescence intensities in SKBR-3 tumors were significantly higher than Colo-205 tumors in 2, 8, 24, and 96 hrs post-injection, respectively. Moreover, the fluorescence images of dissected organs from experimental mice 96 hrs post-injection of MnMEIO-CyTE777-(Bis)-mPEG NPs were acquired for further examination. Fig. 8C showed that strong fluorescence intensity was observed in the SKBR-3 tumor, but was absent in Colo-205 tumor or other dissected organs. Based on these results, strong fluorescence intensity on SKBR-3 tumors was a result of specific binding of MnMEIO-CyTE777-(Bis)-mPEG NPs to both HER2/neu- and EGFR-expressing tumors.
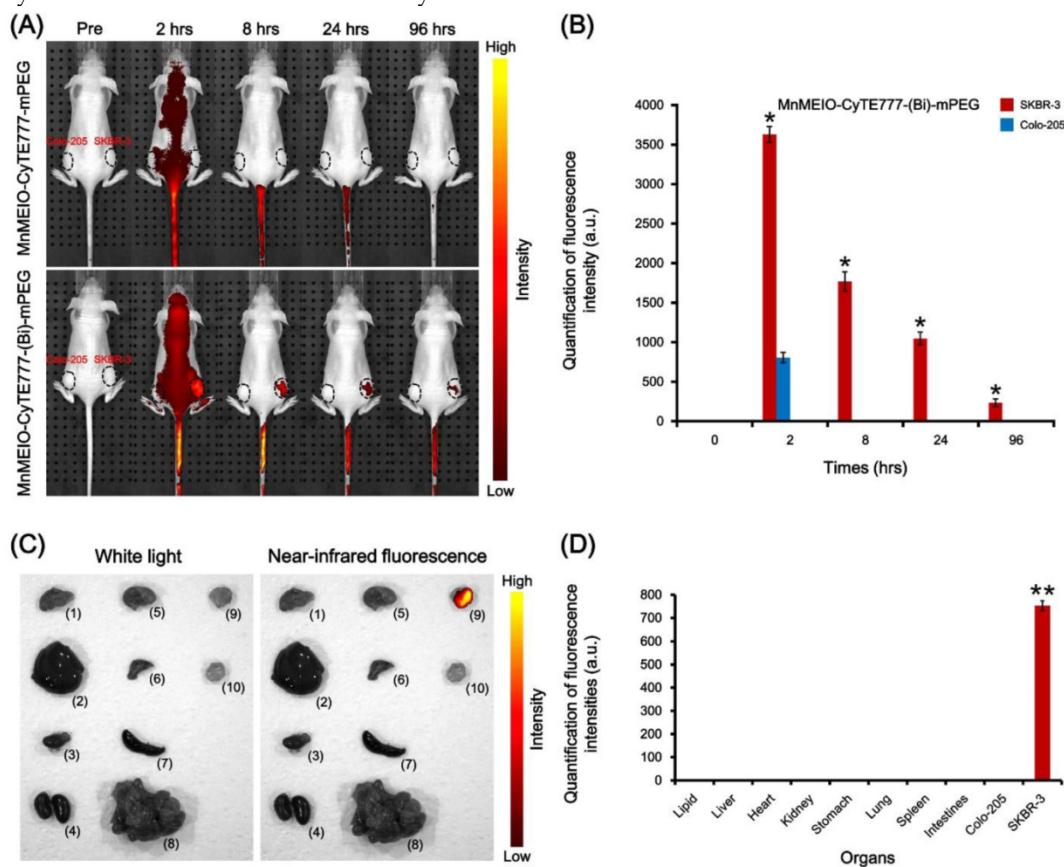

Fig. 8. (A) *In vivo* optical images of nude mice bearing subcutaneous SKBR-3 and Colo-205 tumor xenografts after intravenous injection of MnMEIO-CyTE777-mPEG and MnMEIO-CyTE777-(Bis)-mPEG NPs (10 mg/kg); (B) quantitative fluorescent intensities of the NPs in the tumors with images acquired at pre-injection and various time points (2, 8, 24, and 96 hrs) post-injection; (C) in vivo white light and near-infrared fluorescence images of dissected organs of mice bearing SKBR-3 and Colo-205 tumors sacrificed after 96 hrs post-injection of MnMEIO-CyTE777-(Bis)-mPEG NPs (excitation: 745 nm; emission: 820 nm). (1) lipid, (2) liver, (3) heart, (4) kidney, (5) stomach, (6) lung, (7) spleen, (8) intestines, (9) Colo-205 tumor, and (10) SKBR-3 tumor; (D) quantification of fluorescence intensities of isolated organs.

In vivo MR imaging study

The MR imaging of MnMEIO-CyTE777-(Bis)-mPEG NPs was investigated to test its *in vivo* detection of HER2/neu- and EGFR-expressing tumors. *In vivo* MR imaging study was carried out for MnMEIO-CyTE777-(Bis)-mPEG NPs using nude mice bearing subcutaneous SKBR-3 and Colo-205 tumor xenografts. MR image was measured using T_2-weighted fast spin-echo sequence 7.0 T imaging. The results of *in vivo* MR images are shown in Fig. 9. The negative contrast enhancements were - 62.8 ± 2.7% versus - 5.3 ± 0.2% (2 hrs post-injection) and - 36.9 ± 1.1% versus - 0.6 ± 0.1% (24 hrs post-injection) for SKBR-3 and Colo-205 tumors, respectively. The relative contrast enhancements were 11.8-fold (- 62.8% versus - 5.3%, 2 hrs post-injection), and 61.5-fold (- 36.9% versus - 0.6%, 24 hrs post-injection) higher in SKBR-3 tumors as compared to Colo-205 tumors. The imaging enhancements in SKBR-3 tumors were significantly higher than Colo-205 tumors in both 2 and 24 hrs post-injection, respectively. From these results, it was evident that the higher imaging enhancements indicated more accumulation of contrast agents in SKBR-3 tumors. These data indicated that the highest imaging specificity was observed when MnMEIO-CyTE777-(Bis)-mPEG NPs were used for *in vivo* imaging of HER2/neu- and EGFR-expressing tumors. Moreover, all the above experiments suggested that MnMEIO-CyTE777-(Bis)-mPEG NPs can serve as an efficient and specific target probe for detecting HER2/neu- and EGFR-expressing tumors.

Histological analysis

The aforementioned interpretation is further supported by histological analyses (Fig. 10). Significant localization of MnMEIO-CyTE777-(Bis)-mPEG NPs was founded in SKBR-3 tumor biopsies. In contrast, there was no accumulation of MnMEIO-CyTE777-(Bis)-mPEG NPs in Colo-205 tumor biopsies. These results clearly demonstrate that MnMEIO-CyTE777-(Bis)-mPEG NPs can specifically target to HER2/neu- and EGFR-expressing tumor sites *in vivo*.
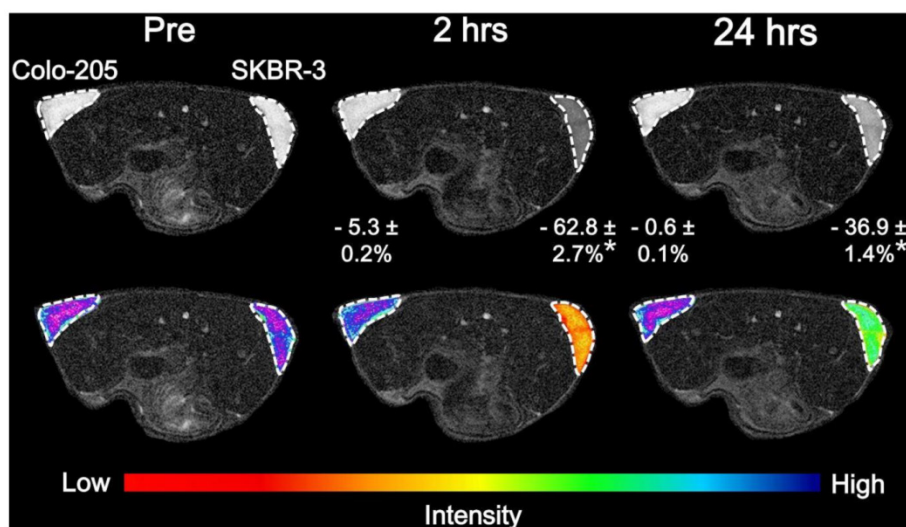

Fig. 9. T_2-weighted MR images (7.0 T) of nude mice bearing subcutaneous SKBR-3 and Colo-205 tumor xenografts before (Pre), and 2 hrs and 24 hrs after injection of MnMEIO-CyTE777-(Bis)-mPEG NPs (10 mg/kg).
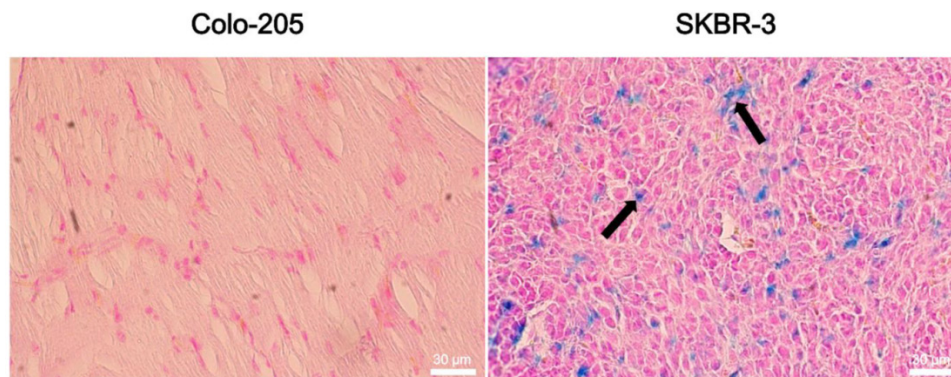

Fig. 10. Histological analyses of (A) Colo-205 and (B) SKBR-3 tumor tissue specimens acquired 96 hrs after injection of MnMEIO-CyTE777-(Bis)-mPEG NPs (10 mg/kg). Sections were stained with Prussian blue. The accumulation of MnMEIO-CyTE777-(Bis)-mPEG NPs is indicated by arrows.

Conclusions

In this study, we have successfully prepared the multifunctional nanoparticles (MnMEIO-CyTE777-(Bis)-mPEG NPs), which containing a near infrared fluorescence dye and the anti-HER2/neu and anti-EGFR bispecific antibody for imaging of HER2/neu- and EGFR-expressing tumors. These nanoparticles could specifically target tumor cells with HER2/neu- and EGFR-expression, making it suitable for either HER2/neu- or EGFR-overexpressing tumor imaging. Based on these results, the potent and specific binding activity of MnMEIO-CyTE777-(Bis)-mPEG NPs points to a promising contrast agent for early diagnoses of HER2/neu- or EGFR-overexpressing cancers.

Supplementary Material

Supplementary Tables and Figures.
http://www.thno.org/v06p0118s1.pdf

Acknowledgements

Competing Interests

The authors have declared that no competing interest exists.

References

1. Liao Z, Wang H, Lv R, et al. Polymeric liposomes-coated superparamagnetic iron oxide nanoparticles as contrast agent for targeted magnetic resonance imaging of cancer cells. Langmuir 2011; 27: 3100-3105.
2. Wu YL, Ye Q, Ho C. Cellular and functional imaging of cardiac transplant rejection. Curr. Cardiovasc. Imaging Rep. 2011; 4: 50-62.
3. Yallapu MM, Othman SF, Curtis ET, et al. Multi-functional magnetic nanoparticles for magnetic resonance imaging and cancer therapy. Biomaterials 2011; 32: 1890-1905.
4. Lu AH, Salabas EL, Schüth F. Magnetic nanoparticles: synthesis, protection, functionalization, and application. Angew. Chem. Int. Ed. 2007; 46: 1222-1244.
5. Lu CW, Hung Y, Hsiao JK, et al. Bifunctional magnetic silica nanoparticles for highly efficient human stem cell labeling. Nano Lett. 2007; 7: 149-154.
6. Hu FQ, Wei L, Zhou Z, et al. Preparation of biocompatible magnetite nanocrystals for *in vivo* magnetic resonance detection of cancer. Adv. Mater. 2006; 18: 2553-2556.
7. Lee JH, Huh YM, Jun YW, et al. Artificially engineered magnetic nanoparticles for ultra-sensitive molecular imaging. Nat. Med. 2006; 13: 95-99.
8. Xie J, Chen K, Lee HY, et al. Ultrasmall c(RGDyK)-coated Fe_3O_4 nanoparticles and their specific targeting to integrin alpha(v)beta3-rich tumor cells. J. Am. Chem. Soc. 2008; 130: 7542-7543.
9. Montet X, Weissleder R, Josephson L. Imaging pancreatic cancer with a peptide-nanoparticle conjugate targeted to normal pancreas. Bioconjugate Chem. 2006; 17: 905-911.
10. Laurent S, Forge D, Port M, et al. Magnetic iron oxide nanoparticles: synthesis, stabilization, vectorization, physicochemical characterizations, and biological applications. Chem. Rev. 2008; 108: 2064-2110.
11. Eberlein C, Kendrew J, McDaid K, et al. A human monoclonal antibody 264RAD targeting $\alpha_v\beta_6$ integrin reduces tumour growth and metastasis, and modulates key biomarkers *in vivo*. Oncogene 2012; 32: 4406-4416.
12. Wicki A, Rochlitz C, Orleth A, et al. Targeting tumor-associated endothelial cells: anti-VEGFR2 immunoliposomes mediate tumor vessel disruption and inhibit tumor growth. Clin. Cancer Res. 2012; 18: 454-464.
13. Kuzucan A, Chen JH, Bahri S, et al. Diagnostic performance of magnetic resonance imaging for assessing tumor response in patients with HER2-negative breast cancer receiving neoadjuvant chemotherapy is associated with molecular biomarker profile. Clin. Breast Cancer 2012; 12: 110-118.
14. Salomon DS, Brandt R, Ciardiello F, et al. Epidermal growth factor-related peptides and their receptors in human malignancies. Crit. Rev. Oncol. Hematol. 1995; 19: 183-232.
15. Byrd JC, Bresalier RS. Mucins and mucin binding proteins in colorectal cancer. Cancer Metastasis Rev. 2004; 23: 77-99.
16. Reichert JM. Antibody-based therapeutics to watch in 2011. MAbs 2011; 3: 76-99.
17. Nelson AL, Dhimolea E, Reichert JM. Development trends for human monoclonal antibody therapeutics. Nat. Rev. Drug Discov. 2010; 9: 767-774.
18. Narayan M, Wilken JA, Harris LN, et al. Trastuzumab-induced HER reprogramming in "resistant" breast carcinoma cells. Cancer Res. 2009; 69: 2191-2194.
19. Jacobsen HJ, Poulsen TT, Dahlman A, et al. Pan-HER, an antibody mixture simultaneously targeting EGFR, HER2 and HER3 effectively overcomes tumor heterogeneity and plasticity. Clin. Cancer Res. 2015; : 3312.
20. Singha NC, Nekoroski T, Zhao C, et al. Tumor-associated hyaluronan limits efficacy of monoclonal antibody therapy. Mol. Cancer Ther. 2015; 14:523-532.
21. Meacham CE, Morrison SJ. Tumour heterogeneity and cancer cell plasticity. Nature 2013; 501: 328-337.
22. Tsutsui S, Ohno S, Murakami S, et al. Prognostic value of the combination of epidermal growth factor receptor and c-ErbB-2 in breast cancer. Surgery 2003; 133: 219-221.
23. Porebska I, Harlozinska A, Bojarowski T. Expression of the tyrosine kinase activity growth factor receptors (EGFR, ERB B2, ERB B3) in colorectal adenocarcinomas and adenomas. Tumour Biol. 2000; 21: 105-115.
24. Bartlett JM, Brawley D, Grigor K, et al. Type I receptor tyrosine kinases are associated with hormone escape in prostate cancer. J. Pathol. 2005; 205: 522-529.
25. Spiess C, Zhai Q, Carter PJ, (in press) Alternative molecular formats and therapeutic applications for bispecific antibodies. Mol. Immunol. 2015.
26. Evans JB, Syed BA, Next-generation antibodies. Nat. Rev. Drug Discov. 2014; 13: 413-414.
27. Laginha K, Mumbengegwi D, Allen T. Liposomes targeted via two different antibodies: assay, B-cell binding and cytotoxicity. Biochim. Biophys. Acta 2005; 1711: 25-32.
28. Eigenbrot C, Fuh G. Two-in-One antibodies with dual action Fabs. Curr. Opin. Chem. Biol. 2013; 17: 400-405.
29. Wu SC, Lin KL, Wang TP, et al. Imaging specificity of MR-optical imaging agents following the masking of surface charge by poly(ethylene glycol). Biomaterials 2013; 34: 4118-4127.
30. Daldrup HE, Link TM, Blasius S, et al. Monitoring radiation-induced changes in bone narrow histopathology with ultra-small superparamagnetic iron oxide (USPIO)-enhanced MRI. J. Magn. Reson. Imaging 1999; 9: 643-652.
31. Soonthornthum T, Arias-Pulido H, Joste N, et al. Epidermal growth factor receptor as a biomarker for cervical cancer. Ann. Oncol. 2011; 22: 2166-2178.
32. Zhou BG, Liu MY, Qiu XC, et al. A novel recombinant immunocasp-6 fusion gene specifically and efficiently suppresses HER2-overexpressing osteosarcoma. Oncol. Rep. 2013; 29: 276-282.
33. Barrajón-Catalán E, Menéndez-Gutiérrez MP, Falco A, et al. Selective death of human breast cancer cells by lytic immunoliposomes: correlation with their HER2 expression level. Cancer Lett. 2010; 290: 192-203.
34. McCluskey AJ, Olive AJ, Starbach MN, et al. Targeting HER2-positive cancer cells with receptor-redirected anthrax protective antigen. Mol. Oncol. 2013; 7: 440-451.
35. Marsh M, McMahon HT. The structural era of endocytosis. Science 1999; 285: 215-220.
36. Murkherjee S, Ghosh RN, Maxfield FR. Endocytosis. Physiol. Rev. 1997; 77: 759-803.
37. Silverstein SC, Steinman RM, Cohn ZA. Endocytosis. Annu. Rev. Biochem. 1977; 46: 669-722.